Spatially resolved photodoping of oxygen-deficient $YBa_2Cu_3O_{7-\delta}$ resonators

Nicolas Lejeune,[1, *] Lukas Nulens,[2] Huidong Li,[3] Thomas Günkel,[3] Lourdes Fabrega,[3] Anna Palau,[3] Joris Van de Vondel,[2] and Alejandro V. Silhanek[1, †]
[1] *Experimental Physics of Nanostructured Materials, Q-MAT,*
Department of Physics, Université de Liège, B-4000 Sart Tilman, Belgium
[2] *Quantum Solid-State Physics, Department of Physics and Astronomy,*
KU Leuven, Celestijnenlaan 200D, Leuven, B-3001, Belgium
[3] *Institut de Ciència de Materials de Barcelona, ICMAB-CSIC, Campus UAB, 08193 Bellaterra, Spain*

(Dated: September 30, 2025)

Oxygen-depleted $YBa_2Cu_3O_{7-\delta}$ exhibits a substantial drop of the normal-state resistivity and an increase of the superconducting critical temperature when illuminated with visible light. The photo-induced states are metastable, slowly decaying at high temperatures and essentially persistent at low temperatures. In this work, we exploit this effect to modify the response of half-wavelength $YBa_2Cu_3O_{7-\delta}$ resonators and simultaneously use the high-sensitivity of the resonant circuit to investigate the persistent photodoping of this material. Under illumination, the bolometric effect and photodoping are clearly distinguished by the different time scales associated with each mechanism. Using a 60 µm-wide laser spot, we were able to locally and reversibly modify the properties of the resonator and demonstrate the position-dependent sensitivity of the device. This enables the direct imaging of standing waves at both the fundamental resonance and the second harmonic.

I. INTRODUCTION

When considering the interaction of electromagnetic waves with conventional superconductors, one encounters a large diversity of physical mechanisms and phenomena, including high reflectivity [1], inverse Faraday effect [2], light-induced superconductivity [3–5], quasiparticle poisoning [6], bolometric (thermal) effect [7, 8], room temperature transient superconductivity [9], photovoltaic effect [10] and many more. Cuprate superconductors behave the same way under short illumination pulses and for low photon doses. However, some cuprates, such as oxygen-depleted $YBa_2Cu_3O_{7-\delta}$ (YBCO), exhibit a striking enhancement of their superconducting properties at much longer illumination times [11]. More concretely, the superconducting transition temperature increases considerably, and the photo-induced change remains after the light has been switched off as long as the sample is kept below certain temperature ($T^* \sim 250$ K). Besides this property, coined persistent photoinduced superconductivity (PPS), there is also an increase of conductivity in the normal state, known as persistent photoinduced conductivity (PPC). For temperatures exceeding T^*, the system relaxes very slowly to its initial conditions. As for the underlying mechanism, after much debate, there seems to be some consensus on the fact PPS and PPC are associated with the presence of oxygen vacancies in the basal CuO chains. Recently, it has been proposed that PPS results from photo-induced oxygen ordering within the CuO chains, leading to a decrease in the electronic scattering rate, whereas PPC can be naturally explained by the excitation of electron-hole pairs followed by electron trapping in the oxygen vacancies and the promotion of holes to the conduction band (photodoping) [12]. This level of control has enabled practical implementations, such as writing Josephson junctions using a scanning near-field microscope [13], demonstrating the method's potential for device engineering.

A particularly suitable technique to investigate the photoresponse of YBCO superconducting systems is through planar transmission line resonators. These circuits can achieve quality factors as high as $Q \approx 10^6$ in low critical temperature superconductors [14, 15] and on the order of $10^3 - 10^4$ in cuprate superconductors [16–18], offering unparalleled sensitivity to minute changes induced by external stimuli or environmental variations [19]. The demonstration of bolometric changes under laser light on superconducting thin films has spurred the use of localized photoresponse as a probe of superconducting resonators by scanning a laser spot across the transmission line. In this technique, an amplitude-modulated laser beam is focused onto the surface of the superconductor, and the absorption of this light results in a modulation of the local temperature. Since the superconducting penetration depth is dependent on temperature, the local penetration depth and thus the local stored magnetic field energy will be modulated [20]. In other words, the effect of illumination is attributed to the photoinduced change of the kinetic inductance due to laser heating. This approach has permitted imaging the local microwave current density in a superconductor [20, 21] and enables tuning the resonant frequency of the resonator with negligible change of the quality factor [22].

The investigations described above were conducted on optimally doped YBCO thin-film resonators, where the low density of oxygen vacancies renders persistent photo-induced effects negligible, making thermal heating

---

[*] nlejeune@uliege.be
[†] asilhanek@uliege.be

the dominant mechanism. In this study, we explore the long-term photo-response of oxygen-depleted YBCO half-wavelength resonators, focusing on the effects of photodoping. This mechanism initially counteracts the bolometric effect and eventually becomes dominant, exhibiting persistent and metastable behavior. By locally illuminating a spot of comparable size as the width of the resonator's track, at the center of the resonator (where the radio-frequency field is strongest), we are able to enhance the resonator's characteristics. This improvement has been previously demonstrated through the introduction of non-uniform columnar defects created by heavy-ion irradiation [23]. Our approach is reversible and enables repeated and multiple comparisons using the same device. This method is applied to map the standing waves at both the fundamental resonance and the second harmonic and complements the bolometric method described in Ref. [8, 24–26].

II. EXPERIMENTAL

Epitaxial $YBa_2Cu_3O_{7-\delta}$ films of thickness 100 nm were grown on top of $(La_{0.3}Sr_{0.7})(Al_{0.65}Ta_{0.35})O_3$ (LSAT) single crystal substrates by pulsed laser deposition. LSAT is a convenient choice due to its low dielectric constant, structural stability, low losses, isotropic microwave response, and it has no twinning [16, 26]. Substrates were heated up to 810 °C, with an oxygen partial pressure of 0.3 mbar and a target-to-substrate distance of 52.5 mm. Ablation of the target material was achieved by using a high fluence laser operating at 2 Jcm^{-2} and a frequency of 5 Hz. During the cooling process to room temperature, the samples were maintained in an oxygen atmosphere of 1 bar. This way, an optimally doped film $\delta \approx 0.1$ with superconducting critical temperature $T_c \approx 90$ K was obtained. A second film was deoxygenated through an ex situ post-annealing process at 400 °C for 4 hours in a 99.5% N_2 atmosphere, leading to a lower oxygen concentration $\delta \approx 0.7$ with superconducting critical temperature $T_c \approx 60$ K [27]. Prior to sample patterning, the T_c of the films was confirmed using a SQUID magnetometer. Both films were patterned by photolithography and wet etching into 8 mm-long 50 Ω $\lambda/2$ resonators with a 20 µm-wide coupling finger-like capacitor, as illustrated in Figure 1(a). The coupling capacitors have been deliberately designed within the weak coupling regime to ensure a quality factor high enough to detect minor changes in the resonance frequency [17]. Generally, the resonance frequency of such a device is given by

$$f_0 = \frac{1}{2l\sqrt{C'L'}}, \tag{1}$$

where l is the length of the resonator, C' is the capacitance per unit length and L' is the inductance per unit length. The latter can be decomposed into two parts $L' = L'_g + L'_k$, with L'_g a constant geometrical part and L'_k a contribution from the kinetic energy of the superconducting electrons. In the framework of the Gorter–Casimir model, the kinetic inductance is given by

$$L'_k(T) = \frac{L'_{k,0}}{1 - (T/T_c)^a}, \tag{2}$$

where $L'_{k,0}$ is the kinetic inductance at zero temperature and a is a fitting parameter that generally ranges from 1.5 to 2 for high-T_c superconductors [28]. The 8 mm-long resonator was designed such that its resonance frequency is close to 5 GHz, with design values $C' = 214.1\ \mathrm{pFm}^{-1}$ and $L'_g = 634\ \mathrm{nHm}^{-1}$. The transmission scattering matrix element $S_{21}(f)$ in the vicinity of the resonant frequency is measured through a vector-network analyzer (Rohde & Schwarz ZNL20). A representative example of $S_{21}(f)$ is shown in Figure 1(c). The asymmetric shape reveals an impedance mismatch [29] which can be fitted using the equation,

$$S_{21}(f) = \left(1 - \frac{Q\left|\hat{Q}_e^{-1}\right| e^{i\phi}}{1 + 2iQ\frac{f-f_0}{f_0}}\right) + Af + B, \tag{3}$$

with Q and Q_e the internal and external quality factors, ϕ a phase factor accounting for impedance mismatch, f_0 the resonant frequency, A and B constants modeling a locally linear background [30]. For the particular example of Figure 1(c), the fitted resonance frequency is $f_0 = 5.153$ GHz ± 2.5 kHz and the quality factor values are $Q = 2128 \pm 4$ and $Q_e = 8.284\ 10^6 \pm 16\ 10^3$, confirming that the resonator is strongly under coupled and that losses are dominated by internal losses. Figure 1(b) shows the evolution of f_0 with temperature for both investigated YBCO resonators. The observed sharp decrease of f_0 as temperature increases is due to the divergence of the kinetic inductance when approaching the superconducting transition. It is precisely this strong temperature dependence that has motivated the use of these devices as sensitive bolometers. In addition, the resonance frequency is also dependent on the magnetic field and magnetic history, as shown in Annex A [18]. Figure 1(d) shows the magnetic field landscape obtained by magneto-optical Faraday rotation technique [31] of the optimally oxygenated resonator at $T = 3.2$ K and under an out-of-plane magnetic field $\mu_0 H_a = 0.6$ mT after zero field cooling. This technique enables probing the degree of uniformity in the superconducting properties, as well as identifying the entry points of magnetic flux.

The experimental setup used to investigate the photoresponse of the planar resonator is shown schematically in Figure 1(a). The sample is mounted inside a closed-cycle optical cryostat, allowing for simultaneous RF measurements, optical imaging, and optical excitation. Two illumination modes are employed. In the widefield illumination mode, a white LED provides broadband light that passes through an infrared blocking filter and a 550 nm bandpass filter

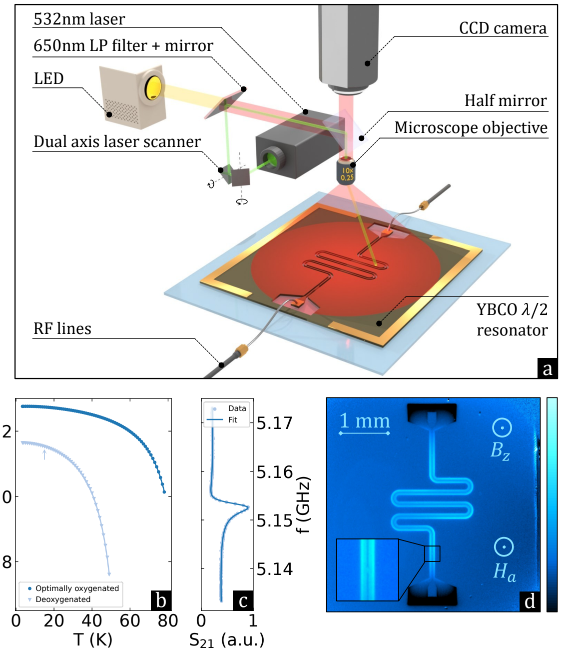

FIG. 1. (a) Schematic representation of the experimental setup that features a double illumination composed of a wide field red-filtered LED used to image the resonator concurrently with a 532 nm laser that is focused on a desired zone of the sample. When photoexciting the entire sample, the 650 nm long-pass (LP) filter and mirror are replaced by a 550 nm bandpass filter, and the laser is not used. (b) Resonance frequency for the optimally oxygenated YBCO resonator and the deoxygenated one. The resonance frequency drops at temperatures close to T_c due to the diverging kinetic inductance. (c) Selected spectrum measured at 15 K on the deoxygenated sample. By fitting the transmission coefficient $S_{21}(f)$ with Eq.(3), it is possible to obtain the resonance frequency for all explored temperatures. At temperatures close to T_c, the uncertainty on the resonance frequency rapidly increases because of the decrease in the intrinsic quality factor. (d) Magneto-optical image of the zero field cooled optimally oxygenated resonator at $T = 3.2$ K and applied an out-of-plane field $\mu_0 H_a = 0.6$ mT. Black color corresponds to local magnetic field with out-of-plane component opposite to the applied field. The inset shows a zoom of the coupling capacitor region, evidenced by the bright spot at the center.

with a 100 nm bandwidth. This filtered light uniformly illuminates the sample. The resulting images are captured using a CCD camera.

In the localized photoexcitation mode, a 532 nm laser beam is steered by a dual mirror scanner and then passes through a carousel of neutral density filters used to modulate its power. The beam is subsequently reflected toward the sample by a 650 nm long-pass filter that features a mirror coating on the side facing the laser. This element reflects the laser beam while also transmitting about 1% of the LED light and filtering its spectrum, thereby combining both light paths without interfering with the laser. The reflected laser beam is then focused onto the sample through a 10× microscope objective, producing a spot approximately 60 µm in diameter. Even though the photoexcitation efficiency is the stronger in the red part of the visible spectrum [32], the photon dose per unit time coming from the laser is about 10^6 times larger than from the red broadband illumination, ensuring that all photoexcitation effects detected are caused by the laser. Images are recorded with the laser beam blanked, using the CCD camera with exposure time adjusted to capture the faint red illumination (see Annex C).

III. RESULTS AND DISCUSSION

1. *Uniform photon irradiation*

The critical temperature for both samples can be extracted from the temperature dependence of f_0 shown in Figure 1(b) by fitting with Eq.(1) and (2). This yields, respectively for the optimally oxygenated and deoxygenated samples, a similar geometrical inductance for both devices of 636.8 ± 0.5 nHm^{-1} and 633.9 ± 1.3 nHm^{-1}, in good agreement with the theoretical value (634 nHm^{-1}) calculated using elliptical integrals for coplanar waveguide (CPW) structures, and a critical temperature $T_c = 90 \pm 0.1$ K and $T_c = 58.1 \pm 0.1$ K. The zero temperature kinetic inductance of the optimally oxygenated sample $L'_{k,0} = 18.1 \pm 0.5$ nHm^{-1} is significantly lower than for the deoxygenated sample $L'_{k,0} = 49.9 \pm 1.4$ nHm^{-1}, manifesting that the latter has a larger sheet resistance and lower superconducting gap.

After characterizing the properties of the deoxygenated sample, the transmission $S_{21}(f)$ was recorded over time every 10 seconds, and the green-filtered LED lamp was switched on for two minutes after the start of the experiment, irradiating the sample with 3.6 mW of 550 nm light. Figure 2(a) shows the time evolution of f_0 at fixed temperature $T = 30\text{ K} \approx T_c/2$. The dose applied over the entire illumination time is estimated to $D = 5 \cdot 10^{21}$ photons/cm^2. As soon as the illumination is switched on, a sharp drop of f_0 is observed (see inset of Figure 2(a)), as a result of the heating caused by the light absorption. The thermally-induced drop takes place on a short timescale of the order of hundreds of milliseconds (see Annex B), and is followed by a recovery with a characteristic time scale of the order of hours, resulting from the photoinduced superconductivity. In this regime, $f_0(t)$ follows a stretched exponential functionality in accordance with previous reports [32, 33], such that the global response of the resonance frequency can be modeled using

$$\begin{aligned} f_0(t) =& f_{0,T} - \delta f_{thermal} \\ &+ \delta f_{PE}\left(1 - \exp\left(-\left(\frac{t-t_0}{\tau}\right)^{\beta}\right)\right), \end{aligned} \tag{4}$$

where $f_{0,T}$ is the dark resonance frequency at temperature T, $\delta f_{thermal}$ is the drop in resonance frequency due to light-induced heating, δf_{PE} is the saturation increment of the resonance frequency due to photoexcitation, $t_0 = 2$ min is the time at which the illumination starts, and β is a dispersion parameter. The fit of the experimental data, shown in Figure 2(a), yields $f_{0,30K} = 5.103$ GHz, $\delta f_{thermal} = 3.77 \pm 0.02$ MHz, $\delta f_{PE} = 14.04 \pm 0.1$ MHz, $\tau = 53 \pm 1.1$ hours and $\beta = 0.497 \pm 0.002$. From the thermally-induced frequency drop, one can infer the temperature load using the previously acquired slope of $f_0(T)$ (Figure 1(b)) yielding a global temperature rise in the superconducting film of about 0.65 K. Furthermore, incorporating the saturation frequency $f_{sat} = f_0 + \delta f_{PE}$, and the obtained geometrical inductance, into Eq.(1), the kinetic inductance at saturation can be estimated as 62.1 nHm^{-1} compared to the initial value of 65.75 nHm^{-1} at 30K. The fact that reaching 95% of the asymptotic state requires continuously photoexciting the sample for approximately 9τ, which in the case of the LED source is about 20 days, makes it highly time consuming to reach the saturation frequency. Repeating the experiment with a higher-power laser source permits reducing the time required to reach saturation without changing the asymptotic value, as the PPS is only a function of the absorbed dose. It is worth pointing out that, unlike most previous investigations of the PPC and PPS based on $R(T)$ measurements, in which the change in T_c or the normal state resistivity is reported, in this work we directly probe the changes in superconducting properties while at sub-critical temperatures.

Persistent photoinduced superconductivity manifests itself as an increase of the superconducting critical temperature. This effect should become visible as the $f_0(T)$ curve shifts towards higher temperatures. In addition, there is also an increase of conductivity in the normal state (persistent photoinduced conductivity), which in turns reduces the zero-temperature kinetic inductance ($L'_{k,0} = \frac{1}{w}\frac{\rho\hbar}{\pi\Delta(0)}$). A manifestation of both these effects is shown in Figure 2(b), in which the temperature dependence of the resonance frequency $f_0(T)$ is measured after 42-hour-long illumination and compared with the response before illumination. The increase in resonance frequency δf_0 resulting from the photoexcitation is shown in Figure 2(c).

2. *Focused photon irradiation*

Once we have characterized the influence of uniform photon irradiation on the deoxygenated YBCO resonator, we proceed to implement focused photon irradiation as a local probe, permitting to map the sensitivity of the device under local excitations. To that end, we focus a laser beam into a 60 µm-diameter spot, which is raster scanned throughout the resonator's surface while tracking the changes in f_0. As a consequence of the large difference in timescales of the bolometric effect and the photoexcitation, they can be discriminated using the protocol illustrated in Figure 3(a). For each laser position, the resonance frequency $f^{(i)}_{0,dark}$ is recorded with the laser blanked. Then, the laser beam is unblanked, and another resonance frequency measurement $f_{0,light}$ is acquired. Eventually, after 60 seconds of irradiation, the laser is blanked again, and the resonance frequency $f^{(f)}_{0,dark}$ is probed one last time. The result of the three-point measurements is shown in Figure 3(b), and the inset emphasizes the slight shift towards higher frequencies of the resonance peak after the photoexcitation. The negative frequency shift, purely due to heating, is given by $\delta f_{thermal} = f_{0,light} - f^{(i)}_{0,dark}$, whereas the photoexcitation-induced shift to higher frequency is given by $\delta f_{PE} = f^{(f)}_{0,dark} - f^{(i)}_{0,dark}$. As shown in Figure 2(a), the time required for the PE to compensate the bolometric effect is of the order of hours, and hence, the PE shift is expected to be orders of magnitude smaller than the one obtained from bolometric effects. On top of the purely electrically probed change, the reflectivity of the sample surface, measured locally using the CCD camera, increases over the same timescale, as discussed in Annex C.

The resulting thermal and photoexcitation maps on the deoxygenated sample, probed at the fundamental frequency for a scanning grid of 40 × 50 pixels over a 2230 × 2790 µm^2 area centered on the resonator, are shown in Figure 3(c,d). A clearly different response is observed through these two methods. Indeed, the thermal response exhibits a more pronounced frequency change in the ground plane, in particular around the mid-point of the resonator, than along the central track and the gap of the resonator. In addition, the excitation and detection lines, capacitively coupled to the resonator, are visible. In contrast to that, the photoexcitation map reveals essentially the central track of the resonator, with the ground plane and excitation/detection feedlines remaining largely insensitive. A similar trend is obtained at the second harmonic $f_1 = 2f_0$ ($l = \lambda$, where λ is the wavelength associated with the resonance frequency), as shown in Figure 3(e,f).

These findings suggest that the thermal response is much broader than the laser spot size due to the heat diffusion in the sample and substrate, whereas the photoexcitation induced directly by the irradiation remains localized. Indeed, numerical modeling reveals that the local temperature at the center of the laser spot increases by approximately 5 K and the thermal spread, characterized by the full width at half-maximum, reaches around 120 µm in diameter. Notably, the initially sharp Gaussian heat source broadens significantly in the thermal response, leading to an increase in temperature of more than 0.5 K across a region 500 µm in diameter, covering roughly one-third of the resonator's surface. The spatial temperature distribution and more details

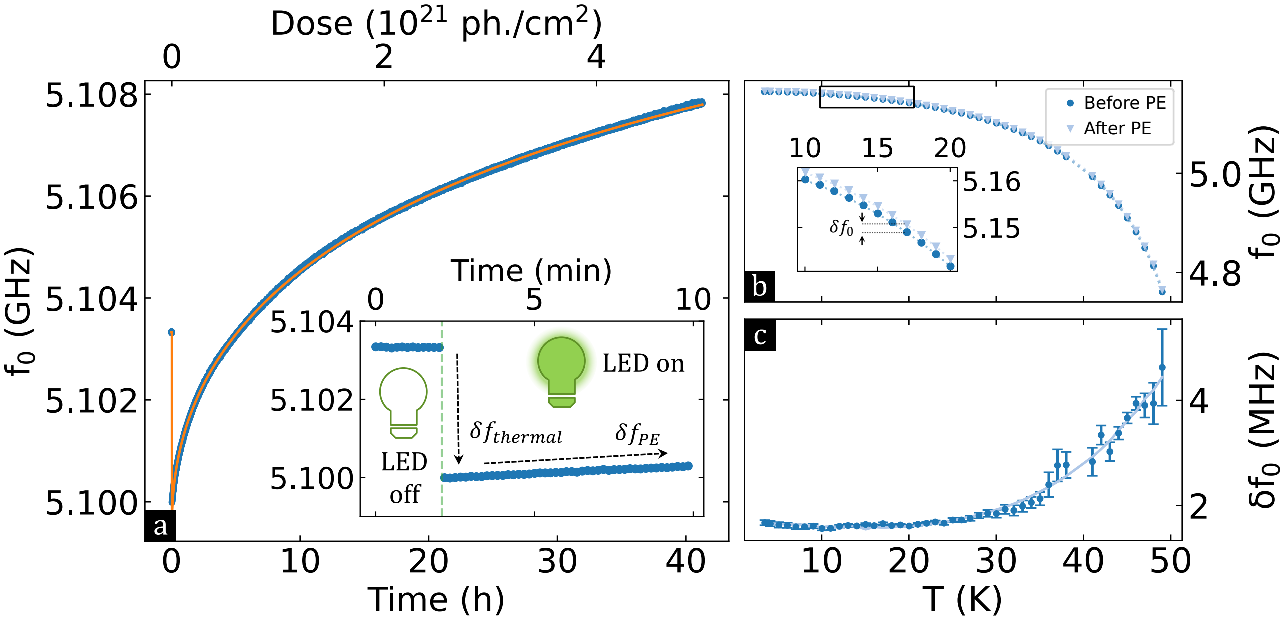

FIG. 2. (a) Evolution of the resonance frequency of the deoxygenated YBCO resonator with time. When a green LED illuminates the sample, starting at $t = 2$ min, the resonance frequency suddenly drops due to the light absorption-induced heating. On a much slower timescale, the resonance frequency increases due to the photoexcitation. (b) Temperature dependence of the dark resonance frequency of the deoxygenated sample before and after illuminating the entire sample with a dose of $D = 5\ 10^{21}$ photons/cm^2. The inset zooms in on the upshift in resonance frequency δf_0. The dashed lines correspond to fits of Eq.(1) to the data points. (c) Frequency shifts extracted from panel (b). For temperatures lower than $T_c/2$, the upshift is constant and approximately 2 MHz, then for higher temperatures it diverges. The solid line correspond to the frequency shift predicted by the fits in panel (b).

about the numerical calculations are provided in the Annex D.

3. Phenomenological Model

A simple model can account for the observed contrasting behavior between bolometric and photoexcitation maps. Indeed, the convolution of physically grounded kernels, i.e. kernels able to describe the mechanisms at play, can faithfully capture the obtained maps. A graphical representation of the phenomenological model described below is presented in Annex E.

The first step consists of identifying the absorption function M_{abs}. For the resonance frequency to be impacted by the irradiation, the laser beam must be absorbed by the sample. Note that the laser irradiation is more absorbed by the superconducting YBCO sample (86%) [34] than by the LSAT substrate (20%) [35]. Therefore, when the laser beam is parked in the gap of the CPW geometry, the sample is substantially less heated, and the change in frequency is attenuated. In contrast, when it sits in the ground plane, the frequency change is accentuated. This is modeled by taking the convolution of the sample geometry $S(x, y)$ with the Gaussian profile from the laser $L(x, y)$. The end result is a qualitative approximation of the quantity of light absorbed at each pixel scanned by the laser, $M_{abs}(x, y) = S(x, y) * L(x, y)$.

Second, we convolve the theoretical current density of the sample $J(x, y)$ with a kernel representing either the bolometric ($G_R(x, y)$) or the photoexcitation effect ($G_r(x, y)$). Here, the argument justifying the use of the current density lies in the fact that measurements are sensitive to changes in L_k', which in turn is correlated to the current density ($L_k' \propto I^2$) [36, 37]. Previous studies have similarly shown that shifts in the resonant frequency can be traced back to the surface magnetic field and, by extension, to the surface current density, thereby confirming that the measured frequency shifts provide insight into the underlying current distribution [24]. To that end, the current density along the resonator's track line is approximated by a sine-like profile with one anti-node for the fundamental mode, and two for the second harmonic. We assume that the current density at resonance is negligible in the rest of the ground plane, which is consistent with simulations. In the case of photoexcitation, since the physical mechanism implies direct absorption of photons without diffusion,

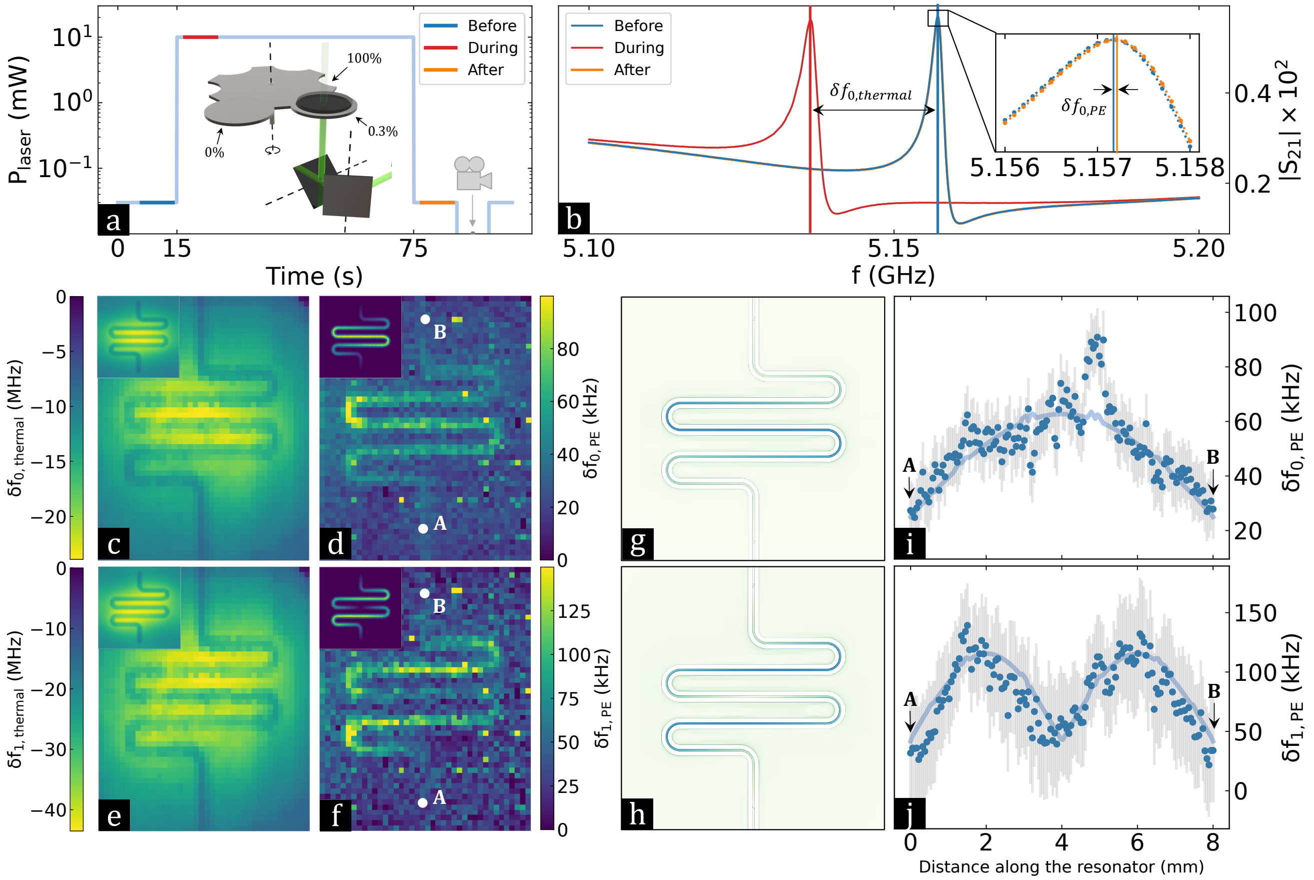

FIG. 3. (a) Schematic representation of the protocol executed at each laser position. Three measurements are performed and synchronized with the unblanking of the laser. At each position, the sample is locally photoexcited for 60 s. A picture is taken using a CCD camera with the laser fully blanked to keep track of the change in reflectivity. The inset shows a schematic view of the neutral density filters carousel used to modulate the laser power by respectively blanking (0%), strongly attenuating (0.3%) or exposing the sample (100%). (b) $S_{21}(f)$ spectra before, during and after the irradiation. The inset is a zoom emphasizing the slight shift of the resonance peak towards higher frequencies after the irradiation. (c) Thermally ($\delta f_{0,thermal}$)- and (d) photoexcitation ($\delta f_{0,PE}$)-induced resonance shift from the fundamental resonance acquired while sweeping the laser over the sample. (e) and (f) are the same maps as panels (c) and (d), but for the second harmonic at double the fundamental frequency. The insets in panels (c-f) show the resulting map obtained using the convolution model described in the main text. (g) (resp. (h)) corresponds to the simulated current density at the fundamental (resp. second harmonic) resonance. (i) and (j) are line profiles following the resonator's shape of the PE shifts for the fundamental and the second harmonic, respectively. The path direction starts at point **A** and ends at point **B** as indicated in the panels (d) and (f). The gray bars correspond to uncertainties in the measured shifts. The continuous blue lines represent the current density extracted from panels (g) and (h).

the convolution uses a Gaussian profile $G_r(x,y)$ of the same size as the laser spot. In contrast to that, for the bolometric response, the kernel corresponds to a function $G_R(x,y)$ reproducing the temperature spread resulting from the finite element simulation. Ultimately, the element-wise products, denoted by $\odot$, given by $M_{\rm abs}(x,y)\odot[J(x,y)*G_r(x,y)]$ and $M_{\rm abs}(x,y)\odot[J(x,y)*G_R(x,y)]$ express the requirement that, for any frequency modification to occur, two conditions must be met simultaneously at each point (x,y): (1) light must be absorbed (as indicated by $M_{\rm abs}$), and (2) the resonator must be sensitive at that location (as described by the convolution $J*G$). The results of these models are presented in the insets of Figure 3(c-f) and qualitatively reproduce the measured maps. The predicted bolometric response even captures the observed broadening of the thermally induced frequency shift region over the whole resonator at $2f_0$, resulting from the fact that the current density is delocalized due to the presence of two anti-nodes in the standing wave. A comparison of the profiles obtained from the experimental data and the phenomenological model can be found in Annex E.

It is worth mentioning that the bolometric response has been extensively investigated as a method to map current distribution in superconducting waveguides and resonators [24, 25]. In this case, in order to achieve high spatial resolution, the laser beam is focused into a $\sim$ 1.5 μm diameter spot, and the laser intensity is modulated at a frequency of about 0.1 MHz to limit the lateral thermal spread to a few µm [24, 26] (see Annex B). This approach is applicable as long as the thermal cycling does not lead to irreversible processes. The present work deals precisely with the metastable process of persistent photoconductivity, and therefore, a lock-in technique based on laser modulation is not a viable option.

As we pointed out above, the photoexcitation is not only able to reveal the standing wave of the fundamental frequency, but also clearly depicts the double anti-node of the current density in the resonator at the second harmonic. Further compelling evidence demonstrating the correlation between the photoexcitation map and the actual current density in the resonator can be obtained through simulations (Sonnet software) of the sample's response at both, the fundamental frequency and the second harmonic. The resonance frequencies obtained for fundamental and second harmonics are 5.05 and 10.02 GHz, without considering the kinetic inductance. The resulting current density maps are shown in Figure 3(g,h). The extracted current density profiles along the resonator are shown in Figure 3(i,j) as a continuous line for both the fundamental and the harmonic, and they are compared with the experimentally determined δf_{PE} data (solid circles). The good agreement between the numerically determined current density and the experimentally measured photoexcitation sensitivity, for both fundamental and second harmonic resonances, validates the interpretation discussed above.

IV. CONCLUSION

In this work, we demonstrated the potential to locally modify the properties of oxygen-depleted YBCO resonators through photodoping. Several key findings merit emphasis. First, unlike traditional bolometric excitation, which is fast, volatile, and highly diffusive, the photodoping process is slow, stable, and non-diffusive. Despite this, it enabled us to map the current density within the resonators, as evidenced by imaging standing waves at the fundamental and second harmonic frequencies. Second, our approach can identify and highlight regions that are more susceptible to changes in the resonator's response. Third, the photodoped areas can be detected via changes in reflectivity using a photodoping-inactive wavelength or low photon doses. While this technique is presented as a proof of concept, with clear opportunities for refinement, particularly in reducing the laser spot size and increasing scanning speed, it demonstrates great promise for direct and erasable laser-based scribing of resonators with tailored precision. Additionally, the proposed technique can be applied to other cuprates exhibiting photoexcitation, such as oxygen-deficient $GdBa_2Cu_3O_x$ [38] and likely $Bi_2Sr_2Ca_2Cu_3O_{10+x}$ [39], and could be extended to study persistent photoconductivity in strontium titanate [40] or lanthanum aluminate [41].

V. ACKNOWLEDGMENTS

The authors acknowledge financial support from Fonds de la Recherche Scientifique - FNRS under the grant Weave -PDRT.0208.23 and the Spanish Ministry of Science and Innovation MCIN/ AEI /10.13039/501100011033/ through the "Severo Ochoa" Programme for Centres of Excellence CEX2023-001263-S, HTSUPERFUN PID2021-124680OB-I00, co-financed by ERDF A way of making Europe. The Nanolito networking project RED2022-134096-T and the Catalan Government with Grant 2021-SGR-00440. The Research Foundation and by COST (European Cooperation in Science and Technology) [www.cost.eu] through COST Action SUPERQUMAP (CA 21144). This research is supported and funded by an interuniversity BOF project (IBOF-23-065). N. L. acknowledges support from FRS-FNRS (Research Fellowships FRIA). This project has received funding from the European Union's Horizon 2020 research and innovation programme under grant agreement No 101007417 having benefited from the access to the facilities of ICN2 - Fundacio Institut Català de Nanociència i Nanotecnologia, Barcelona, (ES) within the framework of the NFFA-Europe Pilot Transnational Access Activity, proposal ID557.

VI. DATA AVAILABILITY

The data that support the plots of this paper and other findings within this study are available from the corresponding author upon reasonable request.

VII. CODE AVAILABILITY

The codes used for this study are available from the corresponding author upon reasonable request.

VIII. AUTHOR CONTRIBUTION

N.L. and A.V.S. conceived the experiment and designed the sample. H.L., T.G., L.F., and A.P. fabricated the device. N.L. conducted all experimental measurements and data analysis. The manuscript was written by N.L. and A.V.S. with contributions from all authors. J.V.V., A.P., and L.N. provided critical proofreading. A.V.S. supervised the research

[1] Kuhr, S. *et al.* Ultrahigh finesse Fabry-Pérot superconducting resonator. *Applied Physics Letters* **90**, 164101 (2007). URL `https://doi.org/10.1063/1.`

2724816.

[2] Mironov, S. V. *et al.* Inverse Faraday effect for superconducting condensates. *Phys. Rev. Lett.* **126**, 137002 (2021). URL `https://link.aps.org/doi/10.1103/PhysRevLett.126.137002`.

[3] Wyatt, A. F. G., Dmitriev, V. M., Moore, W. S. & Sheard, F. W. Microwave-enhanced critical supercurrents in constricted tin films. *Phys. Rev. Lett.* **16**, 1166–1169 (1966). URL `https://link.aps.org/doi/10.1103/PhysRevLett.16.1166`.

[4] Eliashberg, G. M. Film superconductivity stimulated by a high frequency field. *JETP Lett.* **11**, 114 (1970).

[5] Lara, A., Aliev, F. G., Silhanek, A. V. & Moshchalkov, V. V. Microwave-stimulated superconductivity due to presence of vortices. *Scientific Reports* **5**, 9187 (2015). URL `https://doi.org/10.1038/srep09187`.

[6] Testardi, L. R. Destruction of superconductivity by laser light. *Phys. Rev. B* **4**, 2189–2196 (1971). URL `https://link.aps.org/doi/10.1103/PhysRevB.4.2189`.

[7] Sivakov, A., Zhuravel', A., Turutanov, O. & Dmitrenko, I. Spatially resolved characterization of superconducting films and cryoelectronic devices by means of low temperature scanning laser microscope. *Applied Surface Science* **106**, 390–395 (1996). URL `https://www.sciencedirect.com/science/article/pii/S016943329600445X`. Proceedings of the Second International Conference on Photo-Excited Processes and Applications.

[8] Zhuravel, A. P. *et al.* Laser scanning microscopy of HTS films and devices (review article). *Low Temperature Physics* **32**, 592–607 (2006). URL `https://doi.org/10.1063/1.2215376`.

[9] Jang, H. *et al.* Characterization of photoinduced normal state through charge density wave in superconducting $YBa_2Cu_3O_{6.67}$. *Science Advances* **8**, eabk0832 (2022). URL `https://www.science.org/doi/abs/10.1126/sciadv.abk0832`.

[10] Segura-Gutiérrez, L. M. *et al.* Persistent superconductivity and enhanced photovoltaic effect in YBCO thin films under laser irradiation. *The Journal of Physical Chemistry C* **128**, 19329–19336 (2024). URL `https://doi.org/10.1021/acs.jpcc.4c04291`.

[11] Gilabert, A., Hoffmann, A., Medici, M. G. & Schuller, I. K. Photodoping effects in high critical temperature superconducting films and Josephson junctions. *Journal of Superconductivity* **13**, 1–20 (2000). URL `https://doi.org/10.1023/A:1007761805713`.

[12] El Hage, R. *et al.* Disentangling photodoping, photoconductivity, and photosuperconductivity in the cuprates. *Phys. Rev. Lett.* **132**, 066001 (2024). URL `https://link.aps.org/doi/10.1103/PhysRevLett.132.066001`.

[13] Decca, R. S., Drew, H. D., Osquiguil, E., Maiorov, B. & Guimpel, J. Anomalous proximity effect in underdoped $YBa_2Cu_3O_{6+x}$ Josephson junctions. *Phys. Rev. Lett.* **85**, 3708–3711 (2000). URL `https://link.aps.org/doi/10.1103/PhysRevLett.85.3708`.

[14] Tominaga, Y., Shirai, S., Hishida, Y., Terai, H. & Noguchi, A. Intrinsic quality factors approaching 10 million in superconducting planar resonators enabled by spiral geometry. *EPJ Quantum Technology* **12**, 60 (2025). URL `https://doi.org/10.1140/epjqt/s40507-025-00367-w`.

[15] Lozano, D. P. *et al.* Reversing hydrogen-related loss in α-Ta thin films for quantum device fabrication. *Advanced Science* **n/a**, e09244. URL `https://advanced.onlinelibrary.wiley.com/doi/abs/10.1002/advs.202509244`.

[16] Arzeo, M., Lombardi, F. & Bauch, T. Microwave losses in YBCO coplanar waveguide resonators at low power and millikelvin range. *IEEE Transactions on Applied Superconductivity* **25**, 1–4 (2015).

[17] Velluire-Pellat, Z. *et al.* Hybrid quantum systems with high-T_c superconducting resonators. *Scientific Reports* **13**, 14366 (2023). URL `https://doi.org/10.1038/s41598-023-41472-z`.

[18] Roitman, A., Shaulov, A. & Yeshurun, Y. Characterization of $YBa_2Cu_3O_{7-\delta}$ coplanar resonator for microwave kinetic inductance detectors. *Superconductor Science and Technology* **36**, 015002 (2022). URL `http://dx.doi.org/10.1088/1361-6668/ac9eea`.

[19] Nulens, L. *et al.* Noninvasive readout of the kinetic inductance of superconducting nanostructures. *Nano Letters* **24**, 11149–11155 (2024).

[20] Newman, H. S. & Culbertson, J. C. Measurement of the current-density distribution in high-temperature superconducting microstrip by means of kinetic-inductance photoresponse (invited paper). *Microwave and Optical Technology Letters* **6**, 725–728 (1993). URL `https://onlinelibrary.wiley.com/doi/abs/10.1002/mop.4650061303`.

[21] Remillard, S. K. *et al.* Microwave nonlinearity and photoresponse of superconducting resonators with columnar defect micro-channels. *Superconductor Science and Technology* **27**, 095006 (2014). URL `http://dx.doi.org/10.1088/0953-2048/27/9/095006`.

[22] Tsindlekht, M., Golosovsky, M., Chayet, H., Davidov, D. & Chocron, S. Frequency modulation of the superconducting parallel-plate microwave resonator by laser irradiation. *Applied Physics Letters* **65**, 2875–2877 (1994). URL `http://dx.doi.org/10.1063/1.112521`.

[23] Ghigo, G. *et al.* Microwave dissipation in YBCO coplanar resonators with uniform and non-uniform columnar defect distribution. *Superconductor Science and Technology* **17**, 977 (2004). URL `https://dx.doi.org/10.1088/0953-2048/17/8/004`.

[24] Culbertson, J. C., Newman, H. S. & Wilker, C. Optical probe of microwave current distributions in high temperature superconducting transmission lines. *Journal of Applied Physics* **84**, 2768–2787 (1998). URL `https://doi.org/10.1063/1.368390`.

[25] Kaiser, T., Hein, M. A., Müller, G. & Perpeet, M. Spatially resolved microwave field distribution in YBaCuO disk resonators visualized by laser scanning. *Applied Physics Letters* **73**, 3447–3449 (1998). URL `https://doi.org/10.1063/1.122792`.

[26] Zhuravel, A. P., Ustinov, A. V., Harshavardhan, K. S. & Anlage, S. M. Influence of $LaAlO_3$ surface topography on RF current distribution in superconducting microwave devices. *Applied Physics Letters* **81**, 4979–4981 (2002). URL `http://dx.doi.org/10.1063/1.1530753`.

[27] Khallouq, K. *High Critical Temperature Superconducting Oxides of the YBCO System*, 31–57 (Springer Nature Switzerland, Cham, 2024). URL `https://doi.org/10.1007/978-3-031-66238-6_2`.

[28] Vendik, O., Vendik, I. & Kaparkov, D. Empirical model of the microwave properties of high-temperature

superconductors. *IEEE Transactions on Microwave Theory and Techniques* **46**, 469–478 (1998).

[29] Probst, S., Song, F. B., Bushev, P. A., Ustinov, A. V. & Weides, M. Efficient and robust analysis of complex scattering data under noise in microwave resonators. *Review of Scientific Instruments* **86**, 024706 (2015). URL `https://doi.org/10.1063/1.4907935`.

[30] Khalil, M. S., Stoutimore, M. J. A., Wellstood, F. C. & Osborn, K. D. An analysis method for asymmetric resonator transmission applied to superconducting devices. *Journal of Applied Physics* **111**, 054510 (2012). URL `https://doi.org/10.1063/1.3692073`.

[31] Shaw, G. *et al.* Quantitative magneto-optical investigation of superconductor/ferromagnet hybrid structures. *Review of Scientific Instruments* **89**, 023705 (2018). URL `https://doi.org/10.1063/1.5016293`.

[32] Kudinov, V. I. *et al.* Persistent photoconductivity in $YBa_2Cu_3O_{6+x}$ films as a method of photodoping toward metallic and superconducting phases. *Phys. Rev. B* **47**, 9017–9028 (1993). URL `https://link.aps.org/doi/10.1103/PhysRevB.47.9017`.

[33] Stockinger, C., Markowitsch, W., Lang, W., Kula, W. & Sobolewski, R. Mechanisms of photodoping in oxygen-deficient $YBa_2Cu_3O_x$ films studied by in situ transport measurements. *Phys. Rev. B* **57**, 8702–8708 (1998). URL `https://link.aps.org/doi/10.1103/PhysRevB.57.8702`.

[34] Tokizaki, T., Matsuda, K., Nakamura, A., Hirabayashi, I. & Kawamoto, K. Transient induced absorption spectra of YBCO superconductors measured with femtosecond time resolution. In Bando, Y. & Yamauchi, H. (eds.) *Advances in Superconductivity V*, 157–160 (Springer Japan, Tokyo, 1993).

[35] Nunley, T. N. *et al.* Optical constants, band gap, and infrared-active phonons of $(LaAlO_3)_{0.3}(Sr_2AlTaO_6)_0.35$ (LSAT) from spectroscopic ellipsometry. *Journal of Vacuum Science & Technology A* **34**, 051507 (2016). URL `https://doi.org/10.1116/1.4960356`.

[36] Annunziata, A. J. *et al.* Tunable superconducting nanoinductors. *Nanotechnology* **21**, 445202 (2010). URL `https://dx.doi.org/10.1088/0957-4484/21/44/445202`.

[37] Tinkham, M. *Introduction to Superconductivity*. Dover Books on Physics Series (Dover Publications, 2004). URL `https://books.google.be/books?id=VpUk3NfwDIkC`.

[38] Hasen, J. *et al.* Enhancement of persistent photoconductivity in insulating high-T_c thin films. *Phys. Rev. B* **51**, 1342–1345 (1995). URL `https://link.aps.org/doi/10.1103/PhysRevB.51.1342`.

[39] Truccato, M. *et al.* Photoconductivity effects in mixed-phase BSCCO whiskers. *Superconductor Science and Technology* **25**, 105010 (2012). URL `https://dx.doi.org/10.1088/0953-2048/25/10/105010`.

[40] Tarun, M. C., Selim, F. A. & McCluskey, M. D. Persistent photoconductivity in strontium titanate. *Phys. Rev. Lett.* **111**, 187403 (2013). URL `https://link.aps.org/doi/10.1103/PhysRevLett.111.187403`.

[41] Tebano, A., Fabbri, E., Pergolesi, D., Balestrino, G. & Traversa, E. Room-temperature giant persistent photoconductivity in $SrTiO_3/LaAlO_3$ heterostructures. *ACS Nano* **6**, 1278–1283 (2012). URL `https://doi.org/10.1021/nn203991q`.